



Cite this: *Phys. Chem. Chem. Phys.*,
2017, 19, 31436

An insight into intrinsic interfacial properties between Li metals and Li₁₀GeP₂S₁₂ solid electrolytes†

Bingbing Chen,^a Jiangwei Ju,^a Jun Ma,^a Jianjun Zhang,^a Ruijuan Xiao,^{*a}
Guanglei Cui ^{*a} and Liquan Chen^b

Density functional theory simulations and experimental studies were performed to investigate the interfacial properties, including lithium ion migration kinetics, between lithium metal anode and solid electrolyte Li₁₀GeP₂S₁₂(LGPS). The LGPS[001] plane was chosen as the studied surface because the easiest Li⁺ migration pathway is along this direction. The electronic structure of the surface states indicated that the electrochemical stability was reduced at both the PS₄- and GeS₄-terminated surfaces. For the interface cases, the equilibrium interfacial structures of lithium metal against the PS₄-terminated LGPS[001] surface (Li/PS₄-LGPS) and the GeS₄-terminated LGPS[001] surface (Li/GeS₄-LGPS) were revealed based on the structural relaxation and adhesion energy analysis. Solid electrolyte interphases were expected to be formed at both Li/PS₄-LGPS and Li/GeS₄-LGPS interfaces, resulting in an unstable state of interface and large interfacial resistance, which was verified by the EIS results of the Li/LGPS/Li cell. In addition, the simulations of the migration kinetics show that the energy barriers for Li⁺ crossing the Li/GeS₄-LGPS interface were relatively low compared with the Li/PS₄-LGPS interface. This may contribute to the formation of Ge-rich phases at the Li/LGPS interface, which can tune the interfacial structures to improve the ionic conductivity for future all-solid-state batteries. This work will offer a thorough understanding of the Li/LGPS interface, including local structures, electronic states and Li⁺ diffusion behaviors in all-solid-state batteries.

Received 3rd August 2017,
Accepted 8th November 2017

DOI: 10.1039/c7cp05253g

rsc.li/pccp

1. Introduction

With the rapid development of portable wearable devices and electric vehicles,^{1,2} all-solid-state lithium batteries have been extensively studied due to their superior safety, reliability and energy density.^{3,4} It is known that the solid electrolyte plays a critical role in the electrochemical properties of all-solid-state lithium batteries.^{5–7} In practice, solid electrolytes should show high lithium ion (Li⁺) conductivity and chemical stability at the electrode/electrolyte interface to achieve the high energy density and long cycle life of lithium batteries.⁸ Recently, intensive research efforts have found sulfide materials to be promising candidates for solid electrolytes.⁹ Li₁₀GeP₂S₁₂ is capable of transporting Li⁺ with high ionic conductivity

($\sim 1.2 \times 10^{-2}$ S cm⁻¹), comparable to a liquid electrolyte at room temperature.¹⁰ Investigations have attributed the fast ionic conduction behavior to its unique structural characteristics, such as the tetragonal units of PS₄³⁻, GeS₄⁴⁻ and the chained configuration of Li ions.

To understand the fundamental mechanisms of Li ionic conduction, the structural stability and migration pathways in LGPS materials have been analyzed based on density functional theory (DFT).^{11–13} For example, Bhandari *et al.* proposed a novel Li migration mechanism with significantly low energy barriers in the LGPS structure.¹⁴ The relationship between the tetragonal structure of LGPS and isotropic diffusion mechanism with an activation barrier of 0.22 eV determined by experimental methods has been discussed.^{15,16} It is well known that the solid electrolyte must be stable in contact with the anode, as any reaction between the electrolyte and anode will usually lead to degradation of the interface and resistance increases.¹⁷ Therefore, the properties of the electrode/electrolyte interface, especially the resistivity and mechanical stability, directly affect the performance of the all-solid-state batteries. Haruyama *et al.* established the interface model of oxide cathodes and sulfide electrolytes to investigate the space-charge layer effects.¹⁸ Since an Li metal anode is desired for

^a Qingdao Industrial Energy Storage Research Institute, Qingdao Institute of Bioenergy and Bioprocess Technology, Chinese Academy of Sciences, Qingdao 266101, China. E-mail: cuigl@qibebt.ac.cn; Tel: +86-532-80662746

^b Key Laboratory for Renewable Energy, Beijing Key Laboratory for New Energy Materials and Devices, National Laboratory for Condensed Matter Physics, Institute of Physics, Chinese Academy of Sciences, Beijing, China. E-mail: rjxiao@iphy.ac.cn

† Electronic supplementary information (ESI) available. See DOI: 10.1039/c7cp05253g

improving the high-energy density of all solid-state lithium batteries,¹⁹ it is necessary to clarify the phenomena at the interface of LGPS against the Li metal. It had been reported that the formation of Li_2S was found at the Li/LGPS interface.²⁰ In addition, Wu *et al.* considered that the decomposition of LGPS led to the formation of an interphase,²¹ which was composed of Li_3P , Li_2S and Li–Ge alloy. However, there is little research on the Li metal anode and LGPS electrolyte interfacial properties at an atomic level for elucidating the intrinsic mechanism of these reactions.

Herein, we employed first-principles simulations and experimental studies to provide insight into the intrinsic characteristics of the LGPS solid electrolyte and fundamental phenomenon at the interface of LGPS against the Li metal. We studied the local structures and electronic states of LGPS bulk, [001] surfaces and Li/LGPS interfaces. The Li/LGPS interfacial resistance and stability were investigated by experimental study in the Li/LGPS/Li cell. Furthermore, the energy barriers of Li ion migration across the interface along the *c*-direction were well discovered to understand the interfacial resistance. These results will help us to comprehend the mechanisms of stability, Li ion migration and other interfacial properties of the Li/LGPS interface.

2. Computational and experimental methods

2.1 Computational methods

The first principles calculations were performed based on DFT within generalized gradient approximation (GGA) in the Perdew–Burke–Ernzerh (PBE) scheme,²² as implemented in the Vienna ab initio simulation package (VASP).²³ In addition, Projector Augmented Wave (PAW)²⁴ pseudopotentials were used to treat the exchange correlation functionals and electron–ion interactions in our calculations. LGPS shows a 3D framework structure with $P4_2/nmc$ symmetry, and it was found that the disordered distribution and fractional occupancy of PS_4^{3-} and GeS_4^{4-} groups leads to a difficult search for the computation structure models.¹⁰ To make the simulations realizable, the structure with $P4_2$ symmetry, which is the same as that used by Ong *et al.*,²⁵ was adopted in our theoretical calculations. In the simulations, the kinetic energy cutoff was set at 400 eV for the plane wave basis set and the first Brillouin zone integration was generated using the Monkhorst–Pack scheme.¹² The valence electron configurations for elemental constituents were as follows: Li-2s¹, Ge-4s²4p², P-3s²3p³, and S-3s²3p⁴. We used the *k*-point mesh of $3 \times 3 \times 2$ for structural relaxation and the $6 \times 6 \times 4$ *k*-point mesh to calculate the density of states. The nudged elastic band (NEB) method²⁶ was used to obtain the Li ion migrated energy barriers. The energy optimization was considered completed with the conjugate gradient method when a force convergence criterion was less than 0.05 eV Å⁻¹ and the total energy convergence was within 10⁻⁵ eV per unit cell.

In our work, the slab models with a 12 Å-thick vacuum layer were employed to discuss the surface structures to eliminate

the effect between the two image structures due to periodic boundary conditions. In addition, dipole corrections were adopted to avoid the spurious interactions brought by the slab periodic images at the surface calculations. For the interface model, the *k*-point mesh of $3 \times 3 \times 1$ was adopted to relax the interface geometry. In energy relaxation calculations, the atomic coordinates were relaxed and the supercell shape was fixed for the surface and interface calculations. This simulation method has been described in a previous report.²⁷

2.2 Experimental methods

LGPS powders were synthesized based on a solid-state reaction method. For this purpose, Li_2S , P_2S_5 and GeS_2 were mixed in an Ar-filled glove box according to the chemistry composition of $\text{Li}_{10}\text{GeP}_2\text{S}_{12}$. All the reagents were from Alfa Aesar. The powders were sealed into a stainless-steel pot and ball milled for 4 h using a milling instrument (FRITSCH, Pulverisette7). Subsequently, the powders were poured out in an agate mortar and grinded again. The grinded powders were then pressed into pellets, sealed in a tube (Ar filled) and heated at 550 °C for 8 h. After completing the reaction, the pellets were taken out of the tube and ball milled again to obtain the fine LGPS powders. The LGPS pellets used for electrochemical impedance spectroscopy (EIS) and constant DC current polarization testing were fabricated by die pressing the obtained LGPS powders under 300 MPa. The pellets were about 0.4 mm in thickness and 10 mm in diameter. The Li/LGPS/Li symmetrical cells were made into CR2032 coin type.

EIS tests on the Li/LGPS/Li symmetrical cells were first conducted after the cells' fabrication (the fresh sample). After being stored at room temperature for 48 h, EIS of Li/LGPS/Li symmetrical cells were tested again. Then, DC current with a constant density of $\sim 0.5 \text{ mA cm}^{-2}$ was applied to the cells for polarization.

3. Results and discussion

3.1 Structural details and Li ion diffusion in bulk LGPS

The powder X-ray diffraction pattern (XRD) of synthesized LGPS is presented in Fig. 1(a). The simulated XRD for a $P4_2$ -LGPS crystalline structure is also shown for comparison. According to the literature reported by Ong *et al.*,²⁵ the $P4_2/mc$ space group structure has the lowest electrostatic energy among all refined ordered LGPS structures. The relaxed structures and atomic positions of $P4_2$ -LGPS are shown in Fig. 1(b), (c) and Table S1 (ESI†). The calculated diffraction peaks are in agreement with the experimental results apart from little deviation of some peak positions, which results from the disordered Ge/P and Li/vacancy configurations in the real system. In addition, Table S2 (ESI†) shows our calculated and experimental lattice parameters of bulk LGPS, which are consistent with earlier reports ($P4_2$ -LGPS).²⁵ Two kinds of Wyckoff site for Li ions, named 8f and 2c, can be found in the $P4_2$ -LGPS crystalline structure with the tetragonal $P4_2/mc$ space group, as shown in Fig. 1(d). The Li ions at 8f sites line up along the *c*-axis, corresponding to

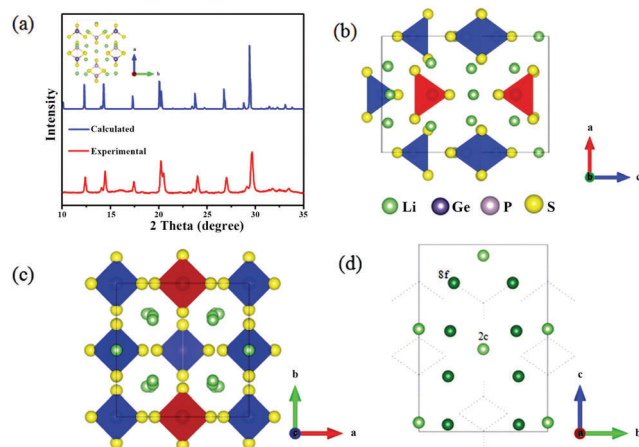


Fig. 1 (a) Experimental and simulated XRD patterns of LGPS and its relaxed $P4_2/mc$ crystal structure viewed along the (b) b -axis and (c) c -axis. (d) The projection of Li ions and Wyckoff sites on the bc plane.

the diffusion in the $[001]$ direction, while the Li ions in the $2c$ sites are responsible for the cross-direction diffusion. The probable pathways for Li ion migration are evaluated by the calculated energy barriers between appropriate Li sites in the $P4_2$ -LGPS.

Previous studies have shown the diffusion of Li atoms in a synchronized way in the LGPS structure along the c -direction because isolated motion of a single Li atom is not feasible along the c -direction.^{14,28} We also used a similar method to calculate the migration energy barriers (the NEB method), and its corresponding diffusion paths for Li ions in $P4_2$ -LGPS are shown in Fig. 2. From Fig. 2(a) and (b), path 1 captures the motion between each of the $8f$ sites and their next vacant site in a synchronized way along the c -direction, while path 2 captures the motion between one $2c$ site to the $8f$ site, and the $8f$ site to

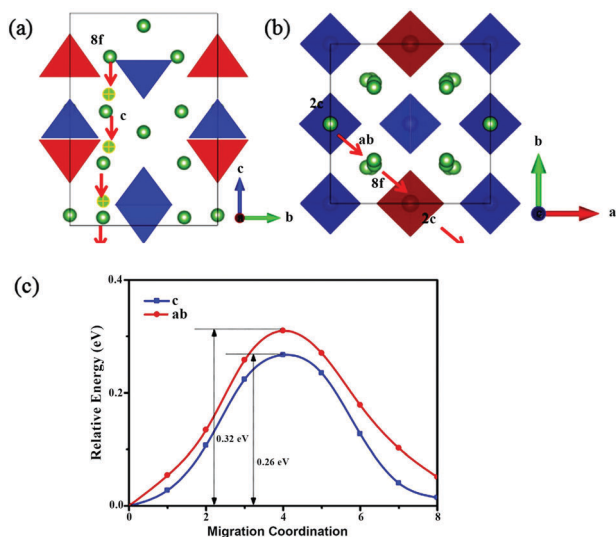


Fig. 2 Illustrated Li ion migration pathways (a) along the c -direction in a synchronized way and (b) in the ab plane with the "knock-off" mechanism, and (c) the energy barriers simulated using the NEB method for these two hopping modes.

the next $2c$ site with a knock-off transport mechanism along the ab plane, which is also shown in Fig. S1 (ESI†). In the $P4_2$ -LGPS structure, the migration barrier (0.32 eV) in the ab plane is higher than that (0.26 eV) along the c -direction in Fig. 2(c). Our results suggest that Li ion diffusion mostly occurred along the $[001]$ direction. Consequently, the diffusion of the Li ion was mainly along the $[001]$ direction for the high ionic conductivity of the solid-state LGPS. We considered an ideal Li ion diffusion in the LGPS structure for the present study. However, studying the region of transient anomalous diffusion and its influence on Li ion migration mechanisms was also interesting. For example, Ghosh *et al.*²⁹ studied this in detail using three-dimensional computer simulations in the lattice of non-inert obstacles. We point out that this study does not deal with the region of transient anomalous diffusion in the LGPS structure, and a more comprehensive study of Li ion diffusion is essential in future research for an LGPS solid electrolyte.

3.2 Properties of the LGPS[001] surface

Before the interface was established, it was crucial to ensure that the surface of LGPS was sufficiently stable. Therefore, the slab supercell of the LGPS[001] surface was constructed from the relaxed bulk $P4_2$ -LGPS. This direction of LGPS[001] was chosen as the studied surface due to its lowest migration energy barrier for the Li ions, according to the method described in previous reports.^{30,31} Two kinds of terminations, PS_4^- and GeS_4^- , were considered for the LGPS[001] surface, as shown in Fig. S2 (ESI†). The middle part of the slabs was fixed during the simulations to reproduce the bulk characteristics. Fig. 3(a) and (b) shows the surface structures after relaxation, and the atomic positions of both relaxed surface structures are also shown in Tables S3 and S4 (ESI†). In both cases, the outermost atoms, constituted by sulphur (S), moved towards the vacuum, leading to a distortion of the PS_4^- and GeS_4^- units and resulting in an increase in the thickness of the slabs. To further understand the electronic properties of the LGPS[001] surfaces, the projected density of states (PDOS) was given at the surface layers in Fig. 3(c). For comparison, the PDOS of bulk $P4_2$ -LGPS, which was reproduced in the surface model, is also shown. The Fermi level was set to 0 eV. From Fig. 3(c), the introduction of a surface affects the electronic structure for the bulk $P4_2$ -LGPS structure, and the conduction band minimum shifts toward lower energy at both

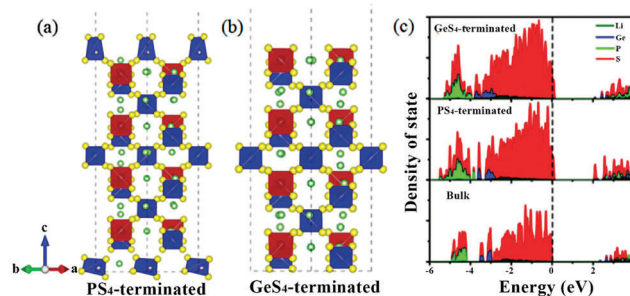


Fig. 3 Relaxed structures of (a) PS_4^- -terminated and (b) GeS_4^- -terminated LGPS[001] surfaces, and (c) partial density of states for these two kinds of surfaces. The PDOS of bulk LGPS is also shown for comparison.

termination surfaces. It is noted that some bands on surfaces are shifted and the gaps are reduced, compared with those in the bulk. In particular, for the PS_4 -terminated case, the lowest unoccupied band was mostly determined by the 3p states of S atoms, with some contributions from Ge atoms, whereas the characteristic narrow peak above the Fermi level mainly consisted of the 3p states of S atoms. As far as we know, the intrinsic redox stability can be evaluated through projected density of states, and the gap of a material may provide an upper limit on its electrochemical window.²⁵ Consequently, our results may suggest that the electrochemical stability of the P_4S_3 -LGPS[001] surfaces may reduce, and these will help us learn more about these surface structures.

In addition, a careful study was performed on the behavior of a single Li atom absorbing on the P_4S_3 -LGPS[001] surface to provide insights into the interaction between Li and LGPS. Two adsorption sites (above the PS_4 and GeS_4 unit, respectively) were chosen to investigate the lithium adsorption behavior on the LGPS[001] surfaces, as shown in Fig. 4, based on fixing the bottom surface layers (five layers). These adsorption sites are labelled as L_{Ge} , L_{P} and L_{Ge}' , L_{P}' . After geometrical optimization, the Li adsorption energies (E_{d}) were calculated for both PS_4 - and GeS_4 -terminated surfaces, which are shown in Fig. 4(c). The Li adsorption energies are given as follows: $E_{\text{d}} = [E_{\text{Li/LGPS}} - E_{\text{LGPS}}(\text{slab}) - E_{\text{Li}}]$, where $E_{\text{Li/LGPS}}$ is the total energy of the Li atom adsorption sites on the surface, and E_{Li} and $E_{\text{LGPS}}(\text{slab})$ are the total energy of the Li atom and LGPS[001] surface, respectively. It was found that the adsorption energy of Li atoms on the GeS_4 -terminated surface was lower than on the PS_4 -terminated surface, which may indicate that the presence of Ge phases at the surface locally improves the stability. In addition, the largest adsorption energy of the Li atom was -1.85 eV for the Li[110] surface,³² and the largest adsorption energy of the Li atom was -2.26 eV for both LGPS[001] surfaces. It is obvious that the adsorption of Li

atoms on the LGPS surface was stronger than on the Li metal [110] surface. These results may suggest that the Li atoms are possibly deposited on LGPS surfaces during the charge process when LGPS is considered as an electrolyte and the Li metal acts as an anode material in the all-solid-state lithium batteries.

3.3 Structure stability at the Li/LGPS interface

Two kinds of interface, Li against GeS_4 -terminated LGPS[001] (Li/ GeS_4 -LGPS) and Li against PS_4 -terminated LGPS[001] (Li/ PS_4 -LGPS), were constructed to investigate the interaction between the LGPS electrolyte and Li metal, as shown in Fig. S3 (ESI†). A similar method of building an interface model was also reported previously.^{18,27} The atomic positions of both relaxed interface structures are also shown in Tables S5–S6 (ESI†). According to the results from Shi *et al.*,³² the Li[110] surface is considered as the exposed area to contact with LGPS. The lattice mismatch is less than 5% between Li[110] and LGPS[001], ensuring the mechanical stability of this interface at the initial stage. To evaluate the binding strength of the interface, the ideal work of adhesion (W_{ad})³³ was calculated as follows: $W_{\text{ad}} = [E_{\text{Li/LGPS}}(\text{total}) - E_{\text{LGPS}}(\text{slab}) - E_{\text{Li}}(\text{slab})]/A$, where A is interface area, $E_{\text{Li/LGPS}}(\text{total})$ is the total energy of the interface model, and $E_{\text{Li}}(\text{slab})$ and $E_{\text{LGPS}}(\text{slab})$ are the total energy of the Li[110] and LGPS[001] slabs, respectively. Fig. 5(b) shows the variation of W_{ad} with different interfacial distances. After structure relaxation, the optimal interfacial distance was obtained. The equilibrium interfacial distance (d_0) was located at the lowest point on the curve of work of adhesion. It can be seen that the GeS_4 -terminated interface exhibited the lower W_{ad} (-1.81 J m^{-2}) and the largest equilibrium interface separation d_0 (2.02 Å). In addition, the PS_4 -terminated interface exhibited a relatively large W_{ad} (-1.57 J m^{-2}), as well as the smaller d_0 (1.82 Å) in Table S7 (ESI†). These results may all be

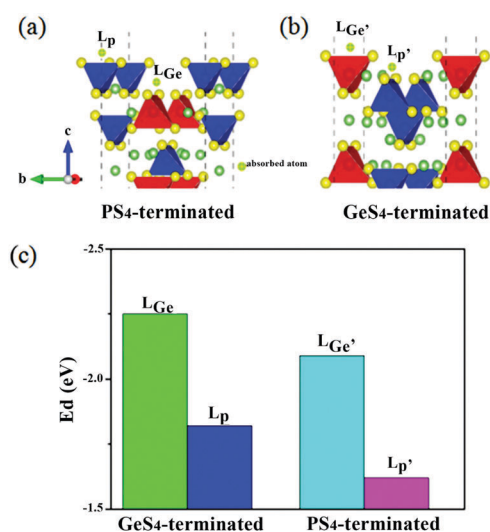


Fig. 4 Li atom adsorption sites on (a) PS_4 -terminated and (b) GeS_4 -terminated LGPS[001] surfaces, and (c) the calculated adsorption energies of an Li atom at different adsorption sites.

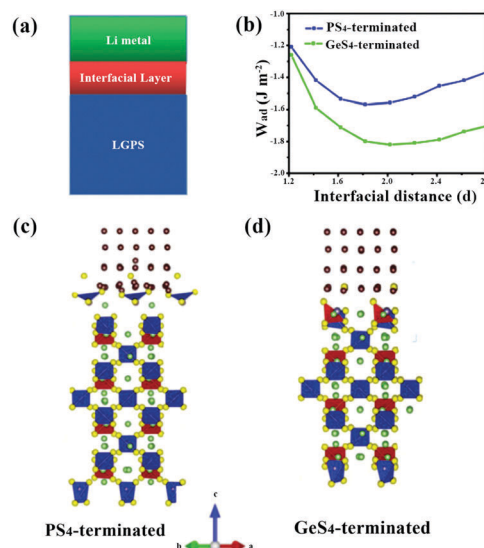


Fig. 5 (a) Sketch map of the Li/LGPS interface. (b) Ideal adhesion energy vs. interfacial distance for both PS_4 - and GeS_4 -terminated systems. The relaxed interfacial structure of (c) the Li/ PS_4 -LGPS interface and (d) the Li/ GeS_4 -LGPS interface.

related to the bonding type of the interfacial atoms. In addition, after the relaxation, Li atoms of the anode were shifted toward the LGPS electrolyte surface side and the S atoms may have moved to the Li metal side, undergoing a relatively small displacement to minimize the energetic mismatch (Fig. 5). It is obvious that the PS_4 and GeS_4 tetrahedral structures were destroyed, resulting in solid electrolyte interphase formation. The present elucidation supports the solid electrolyte interphase formation on the Li/LGPS interface recently proposed by others.^{34–36}

We then investigated the electronic structure of $\text{Li}[110]/\text{LGPS}[001]$ interfaces. The PDOS at the interface layers was examined and the results are shown in Fig. 6(a) and (c). As predicted, it is clear that there are no band gaps in either the Li/PS_4 –LGPS or Li/GeS_4 –LGPS interface system. These interfaces may have had the metallic character, and the electronic states at the Fermi level were mainly attributed to the S atom from LGPS and the Li atom from the Li metal. For both termination cases, bonding interactions between Li s states and S p states were formed according to the hybridization of these states around the Fermi level. For the GeS_4 -terminated case, Li s states contributed a greater percentage than S p states at the Fermi level, and Ge sp states also showed a common peak of Li from the Li metal from -1 to -2 eV. In addition, the Ge sp states exhibited some occupied states at the Fermi level. These signals probably correspond to the formation of bonds between Ge and Li atoms. Furthermore, it was found that P sp states also showed a common peak with Li s states roughly around -2 eV for the PS_4 -termination case, which may, at the interface, indicate hybridization of Li and P sp states, most probably resulting in the formation of Li–P bonds. To deeply understand the behavior of bonding and hybridization at the $\text{Li}[110]/\text{LGPS}[001]$ interfaces, the charge density distributions at the

interface were investigated and these are presented in Fig. 6(b) and (d). It was observed that the electrons appeared around the Li of the lithium metal and s atoms for the both Li/LGPS interface structures. For the GeS_4 -terminated cases, the Ge atoms may have obtained the electron from the Li atoms, resulting in the Ge being reduced. Since Ge is the highest valence (+4) in the LGPS, Ge^{4+} can easily be reduced to lower valence when contacting with the Li metal,³⁷ resulting in the formation of an Li–Ge phase. In both cases, Li atoms transfer electrons toward the LGPS surfaces. Both displayed alignments result in a rather continuous charge accumulation between Li and LGPS at the interface. On the basis of our computations and earlier experimental results,^{37,38} we conclude that solid electrolyte interphases are expected to be formed at the Li/LGPS interface, leading to an unstable interface structure. These results on the atomic scale are in consonance with the experimental observations and clearly indicate the general behavior of the Li metal anode and sulfide solid electrolyte. In addition, the interface atoms of LGPS undergo an obvious metallization, while the layer 2 and layer 3 atoms almost retain their semiconductor nature (Fig. S4, ESI†). Hence, these interfacial metallic characters do not propagate very deeply into the electrolyte in all-solid-state batteries.

To further evaluate the stability issue for this interface, the interfacial properties between metal Li and LGPS were verified using experimental data. EIS tests were first conducted on the fresh $\text{Li}/\text{LGPS}/\text{Li}$ symmetrical cells as shown in Fig. 7a. The interfacial polarization resistance (R_p) was determined to be about $140 \Omega \text{ cm}^2$ (Fig. 7b). After being stored at room temperature for 48 h, R_p increases to over $2000 \Omega \text{ cm}^2$, which is 14 times larger than that of the fresh sample, demonstrating the interface instability between metal Li and LGPS even without any electrochemical processes at room temperature. Subsequently, a DC current with a constant density of 0.5 mA cm^{-2} ($j = 0.5 \text{ mA cm}^{-2}$) was applied to the cell. From Fig. 7c, it can be

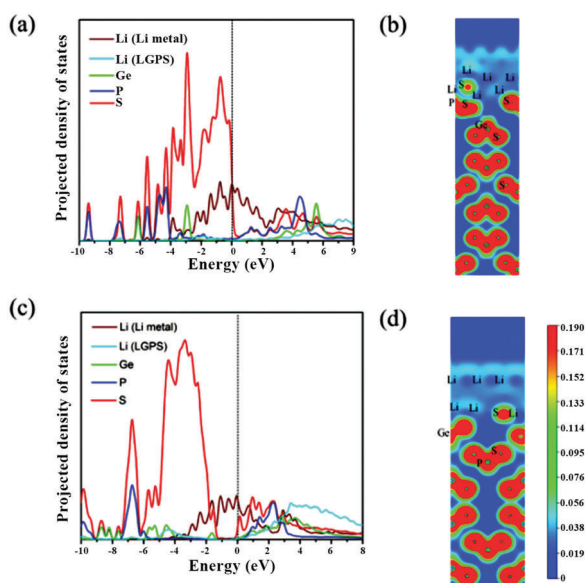


Fig. 6 Projected density of states of both the (a) Li/PS_4 –LGPS and (c) Li/GeS_4 –LGPS interface. The corresponding electron density contour viewed along the 001 direction for the (b) Li/PS_4 –LGPS and (d) Li/GeS_4 –LGPS interface in the unit of $e \text{ Bohr}^{-3}$.

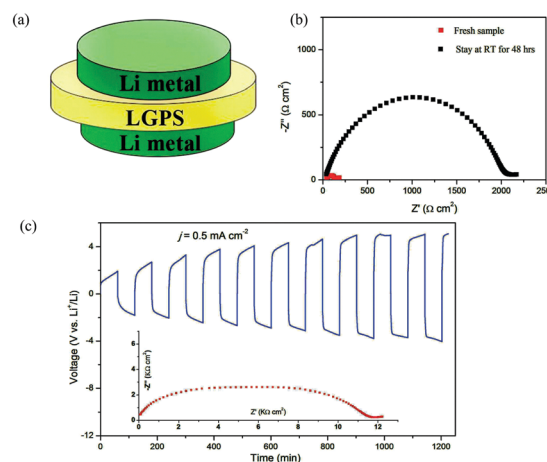


Fig. 7 (a) A schematic view of the $\text{Li}/\text{LGPS}/\text{Li}$ symmetrical cell; (b) EIS results of the fresh $\text{Li}/\text{LGPS}/\text{Li}$ symmetrical cell and after being stored at room temperature for 48 h; (c) DC polarization on the $\text{Li}/\text{LGPS}/\text{Li}$ cell with a constant current density of 0.5 mA cm^{-2} . Inset are the EIS results after polarization.

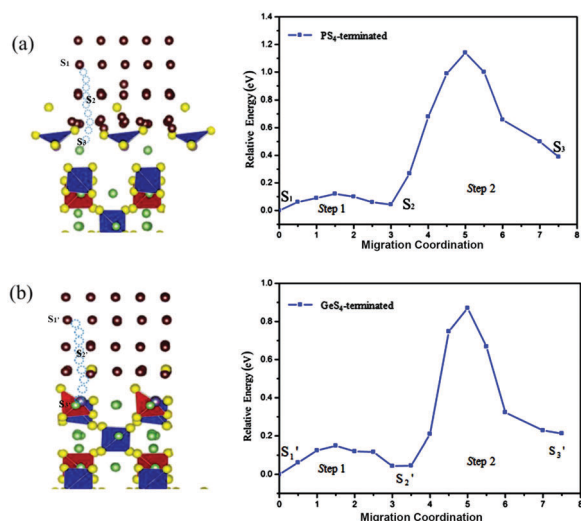


Fig. 8 Li ion migration pathways across the Li/LGPS interface along the c -direction; the energy barriers (right) and paths (left) for Li ion diffusion in the (a) PS_4 -terminated and (b) GeS_4 -terminated interface.

seen that the initial voltage was about 1 V and increased every minute. After 1200 min, the voltage was higher than 5 V and R_p reached a large value, 12 $\text{k}\Omega \text{ cm}^2$. These results directly suggest that the solid electrolyte LGPS interface may be in an unstable state when contacting with the Li metal anode, and solid electrolyte interphases may be generated at the Li/LGPS interfaces, which agree well with the DFT analysis.

3.4 Li ion migration across the Li/LGPS interfaces

To provide a full investigation of the feasibility of Li ions diffusing through the interface, the migration barriers for Li ions across the interface are discussed. In our work, we manually moved one single Li atom from the vacancy to the interstitial position along the c -direction. Therefore, the vacancy and interstitial positions were created in the models; that is, a single lithium vacancy, labelled S1 (or $\text{S1}'$), was created in the $\text{Li}[110]$ layer, and various interstitial sites near to or in the $\text{LGPS}[001]$ layer, labelled as S2 (or $\text{S2}'$) and S3 (or $\text{S3}'$), were considered for two types of terminations as shown in Fig. 8. The migration of Li ions across the Li/LGPS interface was divided into two steps, from S1 to S2 (step 1) and from S2 to S3 (step 2), illustrated by white spheres in Fig. 8(a) and (b). Using the NEB method, the migration energy barriers for lithium ions crossing the interface were calculated. In both cases, the migration of Li^+ from S1 to S2 was relatively easy, and the hopping from S2 to S3 showed much higher barriers and became the controllable step for Li^+ crossing the interface. At the GeS_4 -terminated Li/LGPS interface, the migration energy barrier of step 2 was 0.87 eV, which is smaller than the barrier of ~ 1.20 eV at the PS_4 -terminated interface. This indicates that the presence of GeS_4 -units at the interface locally increases the ionic conductivity, which is in agreement with experimental analyses.³⁸ The migration energy barriers for Li^+ crossing the Li/LGPS interfaces were higher than for Li^+ diffusion in bulk LGPS along the c -direction, indicating that the interfacial resistivity was the main obstacle for Li^+ migration in the all-solid-state batteries.

4. Conclusions

In summary, the LGPS electrolyte was synthesized and the experimental XRD is presented. The structure, electronic states, and kinetic properties of the $\text{Li}[110]/\text{LGPS}[001]$ interface were investigated through DFT calculations. The ground state properties, surface and interface structures, as well as the Li migration mechanism were predicted using first-principles methods. The Li/LGPS interfacial structure was identified at both PS_4 - and GeS_4 -terminated $\text{Li}[110]/\text{LGPS}[001]$ interfaces. The analysis of the electronic structure for $\text{LGPS}[001]$ surfaces demonstrates that the introduction of the $[001]$ surfaces reduced the electrochemical stability. The equilibrium distance between the Li metal and LGPS was investigated to establish the interfacial structures. For both interfacial structures, the analysis of the PDOS and electron density suggests that there is bonding action at the Li/LGPS interfaces and these interfaces are in an unstable state, which may form a solid electrolyte interphase on the LGPS surface. The Li/LGPS/Li cell was also tested to acquire the interfacial resistance and stripping profile. The results exhibit the unstable phenomenon at the Li/LGPS interface, which is in agreement with the theoretical analysis. Finally, corresponding to Li^+ migration pathways at both PS_4 - and GeS_4 -terminated $\text{Li}[110]/\text{LGPS}[001]$ interfaces, the calculated migration barrier energies for Li^+ across the interface were relatively high compared with that in the bulk LGPS along the c -direction. Furthermore, the GeS_4 -terminated interface showed a lower energy barrier for Li ion migrations, which was mainly due to rich Ge phases presented in the interface. These results provide an understanding of the stability of the Li/LGPS interface and diffusion mechanisms for Li^+ across the anode/electrolyte interface. Our calculations on the atomic scale presented here may provide a useful perspective for the design of high-performance lithium metal/sulfide interfaces for the improvement of all-solid-state lithium batteries.

Conflicts of interest

There are no conflicts to declare.

Acknowledgements

This work was financially supported by the National Natural Science Foundation for Distinguished Young Scholars of China (Grant No. 51625204), National Natural Science Foundation of China (No. 51502319), Qingdao Key Lab of Solar Energy Utilization & Energy Storage Technology, China Postdoctoral Science Foundation – Chinese Academy of Sciences (CPSF-CAS) Joint Foundation for Excellent Postdoctoral Fellows, and China Postdoctoral Science Foundation (No. 2017M612366).

Notes and references

- 1 K. Xie and B. Wei, *Adv. Mater.*, 2014, **26**, 3592–3617.
- 2 M. Armand and J. M. Tarascon, *Nature*, 2008, **451**, 652–657.
- 3 W. G. Z. Jürgen Janek, *Nat. Energy*, 2016, **1**, 4.

- 4 X. Su, T. Zhang, X. Liang, H. Gao and B. W. Sheldon, *Acta Mater.*, 2015, **98**, 175–181.
- 5 M. D. Bhatt and C. O'Dwyer, *Phys. Chem. Chem. Phys.*, 2015, **17**, 4799–4844.
- 6 J. Yang, S. Muhammad, M. R. Jo, H. Kim, K. Song, D. A. Agyeman, Y.-I. Kim, W.-S. Yoon and Y.-M. Kang, *Chem. Soc. Rev.*, 2016, **45**, 5717–5770.
- 7 J.-K. Kim, Y. J. Lim, H. Kim, G.-B. Cho and Y. Kim, *Energy Environ. Sci.*, 2015, **8**, 3589–3596.
- 8 J. B. Goodenough and K.-S. Park, *J. Am. Chem. Soc.*, 2013, **135**, 1167–1176.
- 9 R. Kanno and M. Murayama, *J. Electrochem. Soc.*, 2001, **148**, A742–A746.
- 10 N. Kamaya, K. Homma, Y. Yamakawa, M. Hirayama, R. Kanno, M. Yonemura, T. Kamiyama, Y. Kato, S. Hama, K. Kawamoto and A. Mitsui, *Nat. Mater.*, 2011, **10**, 682–686.
- 11 Y. Mo, S. P. Ong and G. Ceder, *Chem. Mater.*, 2012, **24**, 15–17.
- 12 F. Du, X. Ren, J. Yang, J. Liu and W. Zhang, *J. Phys. Chem. C*, 2014, **118**, 10590–10595.
- 13 C. H. Hu, Z. Q. Wang, Z. Y. Sun and C. Y. Ouyang, *Chem. Phys. Lett.*, 2014, **591**, 16–20.
- 14 A. Bhandari and J. Bhattacharya, *J. Phys. Chem. C*, 2016, **120**, 29002–29010.
- 15 A. Kuhn, V. Duppel and B. V. Lotsch, *Energy Environ. Sci.*, 2013, **6**, 3548–3552.
- 16 A. Kuhn, J. Köhler and B. V. Lotsch, *Phys. Chem. Chem. Phys.*, 2013, **15**, 11620–11622.
- 17 X. Yao, D. Liu, C. Wang, P. Long, G. Peng, Y.-S. Hu, H. Li, L. Chen and X. Xu, *Nano Lett.*, 2016, **16**, 7148–7154.
- 18 J. Haruyama, K. Sodeyama, L. Han, K. Takada and Y. Tateyama, *Chem. Mater.*, 2014, **26**, 4248–4255.
- 19 A. Patil, V. Patil, W. S. Dong, J. W. Choi, D. S. Paik and S. J. Yoon, *Mater. Res. Bull.*, 1913, **43**, 1913–1942.
- 20 Y. Zhu, X. He and Y. Mo, *J. Mater. Chem. A*, 2016, **4**, 3253.
- 21 B. Wu, S. Wang, W. Evans IV, D. Z. Deng and J. Yang, *J. Mater. Chem. A*, 2016, **4**, 15266.
- 22 J. P. Perdew, K. Burke and M. Ernzerhof, *Phys. Rev. Lett.*, 1996, **77**, 3865–3868.
- 23 G. Kresse and J. Furthmüller, *Phys. Rev. B: Condens. Matter Mater. Phys.*, 1996, **54**, 11169–11186.
- 24 P. E. Blöchl, *Phys. Rev. B: Condens. Matter Mater. Phys.*, 1994, **50**, 17953.
- 25 S. P. Ong, Y. Mo, W. D. Richards, L. Miara, H. S. Lee and G. Ceder, *Energy Environ. Sci.*, 2013, **6**, 148–156.
- 26 H. Jónsson, G. Mills and K. W. Jacobsen, *Classical & Quantum Dynamics in Condensed Phase Simulations*, 1998, **385**, 385–404.
- 27 S. KC, K. Xiong, R. C. Longo and K. Cho, *J. Power Sources*, 2013, **244**, 136–142.
- 28 M. Xu, J. Ding and E. Ma, *Appl. Phys. Lett.*, 2012, **101**, 031901.
- 29 S. K. Ghosh, A. G. Cherstvy and R. Metzler, *Phys. Chem. Chem. Phys.*, 2015, **17**, 847–858.
- 30 Y. A. Du and N. A. W. Holzwarth, *Phys. Rev. B: Condens. Matter Mater. Phys.*, 2007, **76**, 174302.
- 31 Y. A. Du and N. A. W. Holzwarth, *J. Electrochem. Soc.*, 2007, **154**, A999–A1004.
- 32 L. Shi, A. Xu and T. Zhao, *ACS Appl. Mater. Interfaces*, 2017, **9**, 1987–1994.
- 33 G. Feldbauer, M. Wolloch, P. O. Bedolla, P. Mohn, J. Redinger and A. Vernes, *Phys. Rev. B: Condens. Matter Mater. Phys.*, 2015, **91**, 165413.
- 34 F. Han, Y. Zhu, X. He and Y. Mo, *Adv. Energy Mater.*, 2016, **6**, 1501590.
- 35 R. Chen, W. Qu, X. Guo, L. Li and F. Wu, *Mater. Horiz.*, 2016, **3**, 487–516.
- 36 X. Wang, R. Xiao, H. Li and Q. Chen, *Phys. Chem. Chem. Phys.*, 2016, **18**, 21269.
- 37 M. Sakuma, K. Suzuki, M. Hirayama and R. Kanno, *Solid State Ionics*, 2015, **285**, 101–105.
- 38 S. Wenzel, S. Randau, T. Leichtweiß, D. A. Weber, J. Sann, W. G. Zeier and J. Janek, *Chem. Mater.*, 2016, **28**, 2400–2407.